ChemElectroChem

Articles
doi.org/10.1002/celc.202101191

Chemistry Europe
European Chemical Societies Publishing

www.chemelectrochem.org

Time Resolved Measurements of pH in Aqueous Magnesium-Air Batteries during Discharge and Its Impact for Future Applications

Tobias Braun,* Sirshendu Dinda, Frank Pammer, and Maximilian Fichtner[a]

In aqueous magnesium air batteries, the influence of the electrochemical behavior on pH of the electrolyte has not been investigated yet, which has a critical effect on the cell performance. We have monitored the evolution of the pH at various discharge current densities in situ in the Mg-air primary cells, which produce sparingly soluble magnesium hydroxide (Mg-(OH)$_2$). These experiments show the temporal evolution of the pH of the electrolyte in the cell discharge, depending on the current density. The pH first increases rapidly to a maximum of pH 11 and then drops down slowly to the equilibrium at pH 10.7. At the peak pH oversaturation of Mg(OH)$_2$ is paramount, leading to the precipitation which balances the Mg(OH)$_2$ concentration in the electrolyte. This precipitation process coats both cathode and anode which leads to a decrease in cell efficiency and voltage. The results show that the cell design of Mg-air batteries is important for their lifetime and cell performance. The performance of the aqueous magnesium cell is increased several folds when the design is changed to a simple electrolyte flow cell.

Introduction

Aqueous Mg-air batteries possess some advantages over other primary metal-air batteries.[1,2] Magnesium is non-toxic, environmentally friendly, and the 7th most abundant element on the earth. On the other hand, aqueous electrolytes are cheap and non-flammable, and the air-cathode uses oxygen as a reactant, which is available everywhere.[3,4]

Naturally, there are still some challenges in aqueous Mg-air batteries that are yet to be solved. These include the self-corrosion of the Mg-anode, with the resulting evolution of hydrogen (HER),[3,5–7] and the slow kinetics of the oxygen reduction reaction (ORR) on the cathode.[3] Discharge of Mg-air battery is governed by the following optimal cell reactions, which are also schematically depicted in Figure 1.
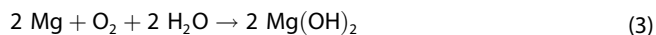
$$Mg \rightarrow Mg^{2+} + 2\ e^- \tag{1}$$

$$O_2 + 2\ H_2O + 4\ e^- \rightarrow 4\ OH^- \tag{2}$$

$$2\ Mg + O_2 + 2\ H_2O \rightarrow 2\ Mg(OH)_2 \tag{3}$$

Figure 1 shows a schematic of a typical aqueous Mg-air battery. During discharge, the magnesium metal anode (Equa-
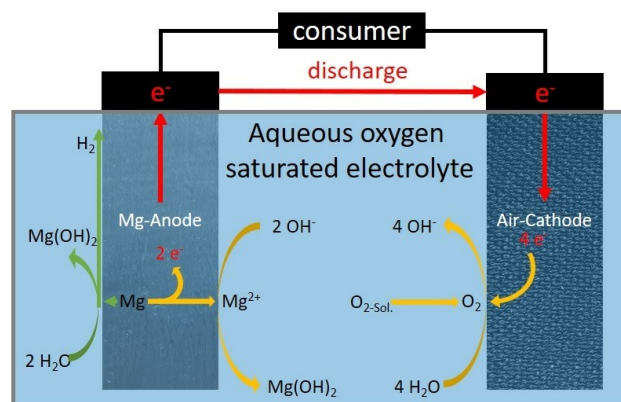

Figure 1. Scheme of an aqueous magnesium air battery.

tion (1)) releases two electrons per atom and Mg^{2+} ions dissolve in the electrolyte solution. The electrons then move from the anode to the air cathode through the external circuit. At the cathode (Equation (2)) oxygen reacts with two water molecules and four electrons to produce four hydroxide anions. Reaction (3) represents the overall cell reaction during discharge. Magnesium hydroxide is formed, which has poor solubility in water (approx. 9 mg L^{-1}) and largely precipitates. Key challenges in the development of Mg–O batteries is the self-corrosion of magnesium in Mg-air batteries, which can be expressed by the following equations

$$Mg \rightarrow Mg^{2+} + 2\ e^- \tag{4}$$

$$2\ H_2O + 2\ e^- \rightarrow H_2 + 2\ OH^- \tag{5}$$

$$Mg + 2\ H_2O \rightarrow Mg(OH)_2 + H_2 \tag{6}$$

[a] Dr. T. Braun, Dr. S. Dinda, Dr. F. Pammer, Prof. Dr. M. Fichtner
Solid-State Chemistry
Helmholtz Institute Ulm
Helmholtzstraße 11, 89081 Ulm, Germany
E-mail: 1.tobias.braun@gmail.com

ChemElectroChem

Articles
doi.org/10.1002/celc.202101191

Chemistry Europe
European Chemical
Societies Publishing

The oxidation of magnesium at the metal surface (4) does not lead to an external current, but rather to direct reduction of water with concurrent release of hydrogen (5). The overall reaction is shown in (6).[3]

To reduce or prevent the HER, magnesium alloys have been investigated as anode materials in Mg-air batteries instead of pure magnesium. Alloys containing Al, Mn, and Zn, help to prevent the hydrogen evolution reaction.[3][8] The Mg−Al−Zn alloy AZ31 is commonly used in Mg-air batteries.[3][9] Other anode alloys with compositions including Li,[10] Pb,[11,12] Ca,[13,14] Ce,[12,15] Sn,[16,17] In,[11] Cd[18–20] and Y[12,21] have also been investigated regarding their discharge and corrosion behavior. These investigations include the effect of temperature during alloy manufacturing on the discharge behavior.[16]

The air-cathode is a combination of a gas diffusion layer and a catalyst material, which is required to accelerate the slow kinetics of the ORR. Many catalysts are available for the oxygen reduction reaction (2) due to the fact, that this reaction is similar to the half-cell reaction in a fuel cell, and it is known that this is one of the most critical parameters in aqueous metal-air systems. Substantial effort has been invested into the development of more efficient, stable and cheap catalysts for the oxygen reduction reaction. These catalysts can be divided into three main categories: (1) Precious metal catalysts that include Pt,[22–27] Pd,[28–30] Au,[31–34] Ag[35–37] and their alloys.[38,39] They exhibit good catalytic activity but are invariably costly; (2) Non-precious metal catalyst include transition metals[40–42] and their alloys,[43] oxides,[44,45] carbides[46] and nitrates.[47,48] Most frequently Mn,[44] Ni,[42] Fe,[44] Co[42] are used. These are cheaper as category (1) materials, but they have a lower catalytic activity and higher overpotentials; (3) Metal-free catalysts mainly composed of activated carbon. To increase the catalytic activity of the carbon the material is typically modified via hetero atom doping with B,[49–51] N,[52–54] O,[55,56] F,[57–59] P[60–62] and S[63,64] or co-doping.[65–67] These materials are cheap and show a good electric conductivity.

Depending on the pH of the electrolyte, the ORR has different reaction pathways. There is the preferred one-step-four-electron pathway shown in reaction (2), but an undesirable two-step-two-electron pathway is also possible, as shown in reactions (7) and (8).[68,69]

$$O_2 + H_2O + 2\ e^- \rightarrow HO_2^- + OH^- \tag{7}$$

$$HO_2^- + H_2O + 2\ e^- \rightarrow 3\ OH^- \tag{8}$$
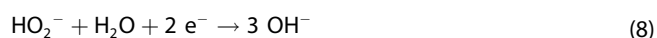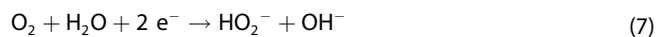
The catalyzed reaction most frequently proceeds via the undesirable two-step-two-electron pathway.

The most commonly used electrolyte is a 3.5 wt% aqueous NaCl solution, but other concentrations have also been used. Likewise, studied were other salts (NaNO3, NaNO2, Na2SO4, NaOH or MgCl2,[3,70] and the use of various additives as corrosion inhibitors.[71–75]

Aqueous magnesium-air batteries are already in use in commercial applications such as emergency energy backup systems and in as power supply in marine installations and devices such as lighthouses, floats, and undersea monitoring equipment.[3] The Canadian company Magpowersystems Inc. tries to commercialize magnesium-air batteries for various marine, military and consumer applications.[76]

On aspect of MABs that has not yet been examined, however, is the time-resolved evolution of the pH during discharge. It is known from the literature that the cell reaction product Mg(OH)2 is not sufficiently soluble in in water and hence increases the pH of the electrolyte over time. In this work, we investigate the temporal evolution of pH of a 0.5 molar NaCl electrolyte during the discharge of aqueous magnesium-air batteries in home-made cells. Here we have discussed the origin of the pH, examined the time dependent behavior of the pH and linked it with the cell potential of the primary magnesium air cell. We have discussed the performance of the cell in regards to Mg(OH)2 precipitation and have designed an alternative way to enhance the primary cell performance. AZ31 is used as anode and Freudenberg GDL/MPL with a Pt/C (5 w.-% Pt) catalyst are used as cathode.

Results and Discussion

In a first series of experiments, the discharge behavior of 'stationary' cells was investigated, with a fixed volume of aqueous 0.5 M NaCl as electrolyte (see Figure S1 in the electronic supporting information (ESI)). Figure 2 shows pH mean curves during OCV (a) and discharge with three different current densities (b: 1, c: 2.5 and d: 5 mA cm^{-2}) for 5 hours. It is obvious that all pH curves are showing a maximum pH value at 10.7. The time at which the maximum pH is reached varies with the discharge current density (higher current densities leads to earlier time points and the volume of the electrochemical cell). In all cases, there is a fast increase of the pH in the first 5 minutes from 6 to around 10. In the OCV-measurement the increase of the pH results from the self-corrosion of the magnesium. During discharge, the cathode reaction leads to a formation of OH$^-$ which is mainly responsible for the change in pH. The fact that the pH decreases again after a certain time indicates a precipitation of the discharge product magnesium hydroxide (Mg(OH)2). The pK$_a^1$ value of Mg^{2+} ions in aqueous solution (i.e. [Mg(H$_2$O)$_6$]$^{2+}$) is 11.4,[77,78] which means solvate complexes of Mg^{2+} cations are non-acidic and self-corrosion will therefore lead to an increase of the pH of the solution. In addition, it has been demonstrated that the degradation of Mg is linear at low pH, whereas the breakdown potential follows a quadratic law at pH higher than 10. In time of breakdown, it has been postulated that an oxide/hydroxide protective layer is formed on top of the Mg/Mg-alloy surface. Concentration of Cl$^-$ ([Cl$^-$]) plays an important role, both as a thinning catalyst and equilibrium pH stabilizer.[79,80] The formation of Mg(OH)2 at higher pH attributes to the low solubility product (K$_{sp}$) value of Mg(OH)2. K$_{sp}$ of Mg(OH)2 is 5.61×10^{-12} under ambient condition, which leads to a pH of 10.35 when Mg(OH)2 starts to precipitate from the saturated solution. But K$_{sp}$ of Mg(OH)2 depends on the logarithm of [Cl$^-$] as shown in equation (9).[80]

ChemElectroChem

Articles
doi.org/10.1002/celc.202101191

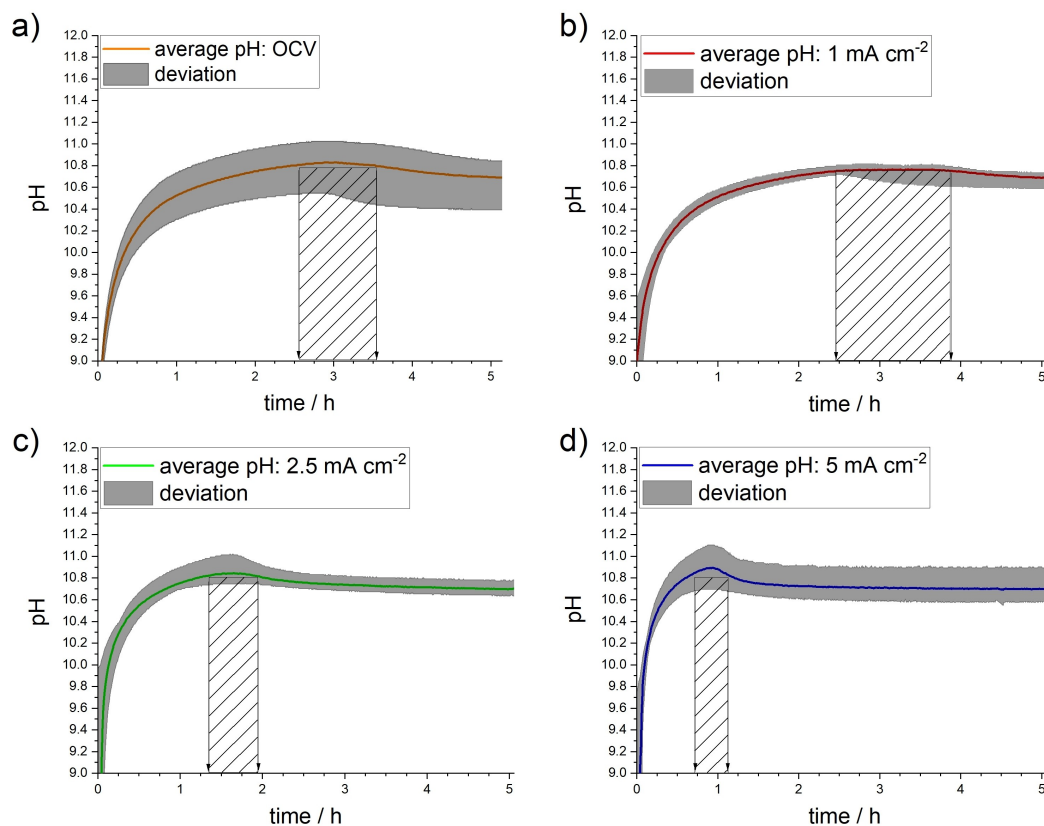**Chemistry Europe**
European Chemical
Societies Publishing

Figure 2. Curves of the pH mean during discharge with different current densities a) OCV, b) 1 mA cm^{-2}, c) 2.5 mA cm^{-2} and d) 5 mA cm^{-2}.

$$K_{sp} = K^1_{sp} + 4.8 \times 10^{-11} \, \log_{10}[Cl^-] \qquad (9)$$

Wherein $K^1_{sp} = 1.2 \times 10^{-11}$ M^3 is the solubility product of Mg(OH)$_2$ measured in 1 M NaCl solution. For a 0.5 M solution of NaCl the pH corresponds to 10.7. Mg(OH)$_2$ has a poor solubility in water of 9 mg L^{-1} and can precipitate everywhere in the cell. The formation of a Mg(OH)$_2$-layer on the Mg anode creates a protective layer which is still permeable for Mg-ions and reduces anode corrosion. In contrast, at the cathode a Mg(OH)$_2$-layer leads to a loss of activity. If the catalyst is blocked by a passivation layer of Mg(OH)$_2$, no further oxygen can be reduced, because it cannot be adsorbed on the active surface. As a result, the cell potential of the magnesium air battery starts to decrease. This effect is shown in Figure 3. Here we can correlate the discharge curves with the slope of the pH curves for the different current densities. The slope of the cell potentials shows a small plateau at the beginning of the discharge (depending on the current densities: between 40 and 15 minutes), which corresponds to oxidation of the freshly polished magnesium-anode surface. Afterwards the voltage decreases by 2.1 to 2.6%, because of the formation of a Mg(OH)$_2$-layer on the anode. The cell potential is stable until the pH reaches its maximum after 65 to 135 minutes, and then drops rapidly as the Mg(OH)$_2$ starts to precipitate everywhere in the cell. At this point there is a huge voltage drop, especially at higher discharge current densities. Further examples at different discharge current densities are shown in Figure S3, Figure S4, Figure S5 and Figure S6 in the ESI.

The Mg^{2+}-concentration of the electrolyte was determined via ICP-OES measurements. The results show an interesting behavior, at the beginning of the discharge, the Mg-concentrations are higher than calculated, by additional dissolved Mg^{2+} due to corrosion, as shown in Figure 4. Depending on the discharge current densities, the experimental Mg concentration (—■—) drops below the values predicted without precipitation (— ·) and eventually also below those predicted without corrosion (— —). The timing of this crossover correlates with the maximum pH (★). This behavior can be explained by the precipitation of Mg(OH)$_2$. As Table 1 shows a timing of the maximum pH-maximum lies near to or within the time ranges of the concentration drop and the voltage drop for the different current densities used. This correlation points towards an oversaturation of the solution with Mg(OH)$_2$ and its subsequent

Table 1. Comparison of the time points of the different parameters for the current densities 1, 2.5 and 5 mA cm^{-2} and OCV.

Current density / [mA cm^{-2}]	Time point of pH maximum / [min]	Time point of concentration drop region / [min]	Time point of voltage drop region / [min]
1	144.167 ± 30	120–180	140–145
2.5	80.843 ± 17.9	45–120	94–113
5	42.5 ± 12.5	35–45	32–54
OCV	180 ± 30	180–240	–

ChemElectroChem

Articles
doi.org/10.1002/celc.202101191

Chemistry
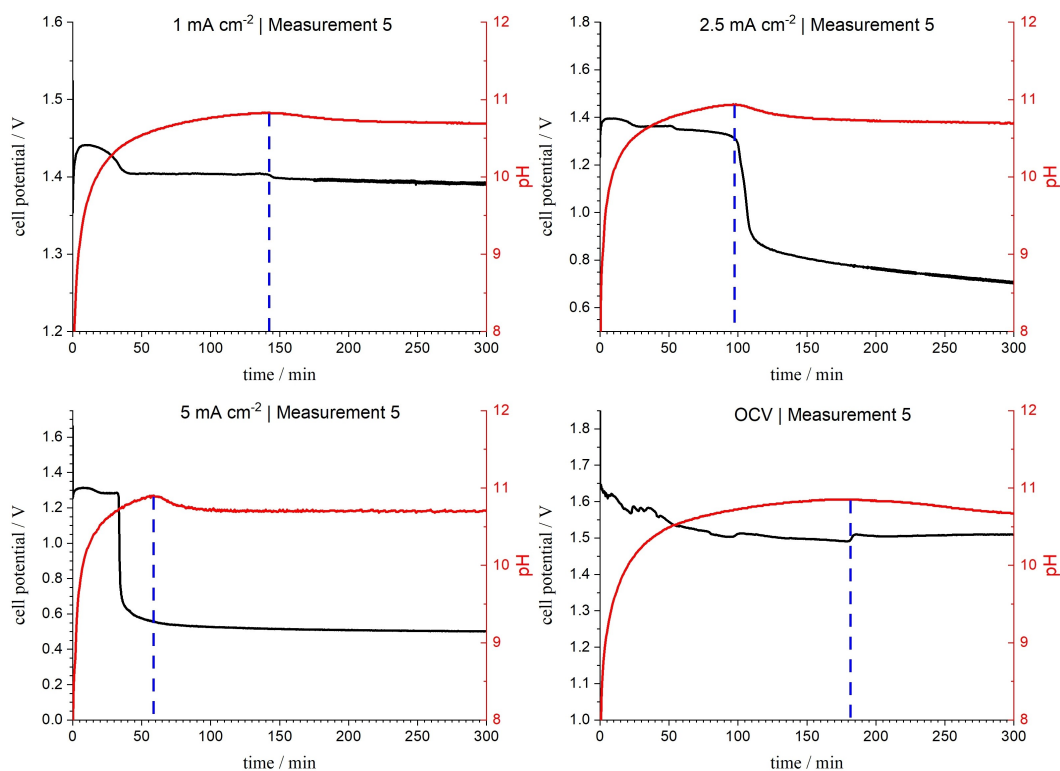**Europe**
European Chemical
Societies Publishing

Figure 3. Correlation between slope of pH and discharge curves.

precipitation. It is obvious, especially at higher current densities, that the voltage drop begins already before reaching the maximum pH. In these cases, there is a large difference in the Mg-concentrations at the electrode surface and in the bulk solution. This concentration gradient leads to an earlier voltage drop, because of high concentrations of Mg^{2+} and OH^- in the immediate vicinity of the electrodes, which leads to local precipitation of $Mg(OH)_2$ on the electrode surfaces.

Figure 5 shows powder X-ray refractograms of a) pristine anode AZ31 and b) pristine cathode Pt/C and of electrodes after discharge. AZ31 shows the peaks typical for this alloy. Electrodes discharge at different rates and under OCV-conditions all show newly emerging patterns, which are attributed to reflexes of the discharge product $Mg(OH)_2$.[81] The pristine cathode shows a carbon peak at 25.2° ([002]), as well as reflexes assigned to platinum at 44.3° ([200]), 64.6° ([220]) and 81.9° ([311]). Each pattern of the used cathodes shows two phases, which are assigned to NaCl and $Mg(OH)_2$. The results by XRD showed that the discharge product $Mg(OH)_2$ is observable on both electrodes after discharge and under OCV-conditions. As discussed before, the $Mg(OH)_2$-film that precipitates on the cathode can block the catalyst and leads to a performance drop of the battery cell.

SEM and EDX confirm the previous results. Figure 6 shows SEM images of the cathode after discharge and OCV. At all current densities the cathodes are coated with a thick layer of discharge products with a Mg to O ratio of approx. 1:2 which belongs to $Mg(OH)_2$ and Na to Cl ratio of approx. 1:1 which belongs to electrolyte salt. The $Mg(OH)_2$-layer on the cathode

during OCV is less thick and the elemental analysis shows additional signals from the Pt-catalysts and the Nafion binder (see Figure S7 in the ESI for image of pristine electrode). The $Mg(OH)_2$-layer on the cathodes shows a lamellar morphology.[82]

Figure 7 shows SEM images of the anode after discharge and OCV. The anodes show two different types of morphology. There is a needle like structure with a higher chloride content (approx. 10 At-%) and an agglomeration of small particles of discharge products with a Mg to O ratio of approx. 1:2 which is thereby identified as $Mg(OH)_2$.

As an alkaline earth metal hydroxide, $Mg(OH)_2$ adopts the space group to P3 m1, where every Mg atom is symmetrically coordinated by two OH groups. Raman spectra of powdered $Mg(OH)_2$ show of three distinct peaks located at 279.5, 444.9 and 3653.1 cm^{-1}. The bending mode of Mg-OH (E_g) contributes to the first peak, whereas a combination of two degenerate modes, A_{1g} (symmetric stretching) and E_g^{OH} (bending of —OH group), gives rise to the second peak. On the other hand, the high frequency mode at ~3650 cm^{-1}, is attributed to the A_{1g}^{OH} out-of-plane breathing mode of —OH groups.[83,80] The Raman spectra (Figure 8) clearly indicate that there is $Mg(OH)_2$ present on both anode and cathode when after they have been exposed to the cell environment for longer periods of time. The low-frequency peaks do not provide any information about the morphology of the layers formed on the electrodes, as these vibrations are not participating in the stacking of $Mg(OH)_2$ layers, as the $Mg(OH)_2$ layers get closer to monolayer these bands vanish.[83] It is clear from the Raman spectra (Figure 8 (b)) that the layer formed on top of the cathode material is very
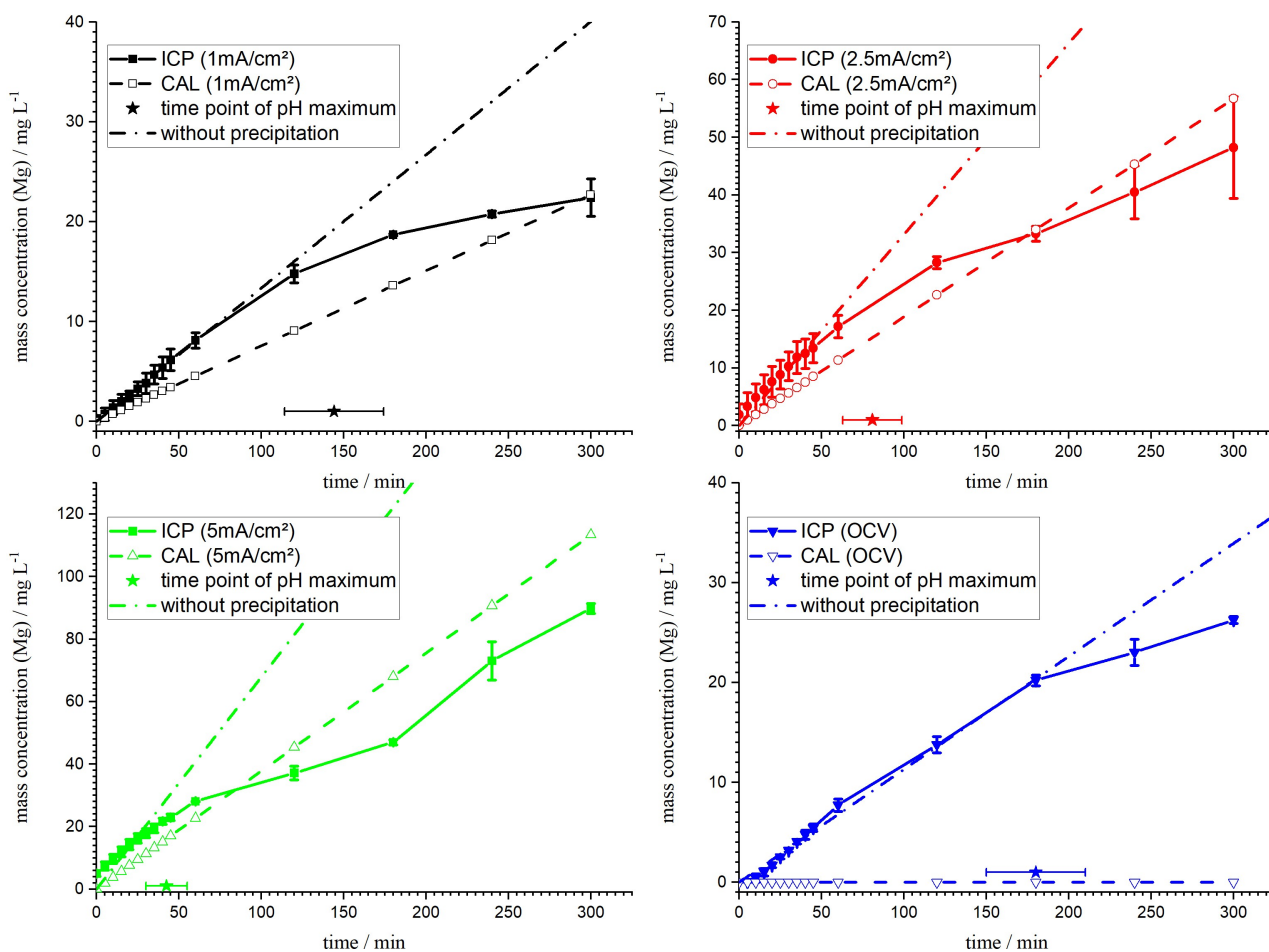
ChemElectroChem

Articles
doi.org/10.1002/celc.202101191

Chemistry Europe
European Chemical
Societies Publishing

Figure 4. Correlation between Mg-concentration determined by ICP-OES, theoretical Mg-concentration without corrosion and the predicted concentration without precipitation with the time point of pH maximum.
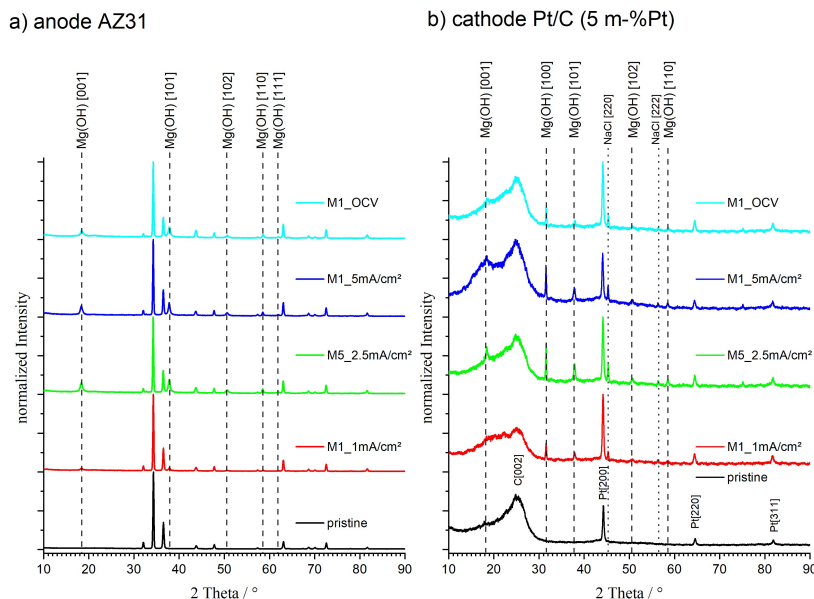

Figure 5. Powder X-Ray refractograms of a) anode AZ31 and b) cathode Pt/C after cell tests. Dashes (—) and dots (···) indicates peaks attributed to $Mg(OH)_2$ and NaCl, respectively.
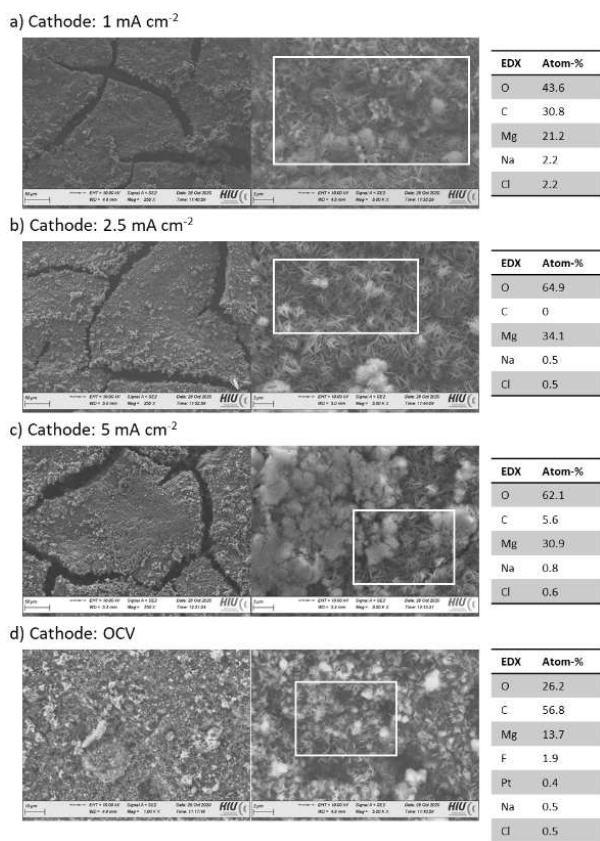
ChemElectroChem

Articles
doi.org/10.1002/celc.202101191

Chemistry
Europe

European Chemical
Societies Publishing

Figure 6. SEM images of the cathode after discharging with a current density of a) 1 mA cm^{-2}, b) 2.5 mA cm^{-2}, c) 5 mA cm^{-2}, and OCV including elemental-analysis (EDX).
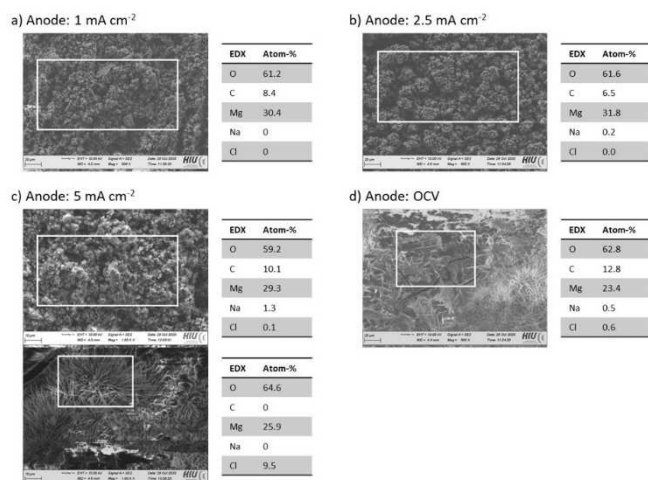

Figure 7. SEM images of the anode after discharging with a current density of a) 1 mA cm^{-2}, b) 2.5 mA cm^{-2}, c) 5 mA cm^{-2}, and OCV including elemental-analysis (EDX).

Figure 8. Raman spectra of a) anode AZ31 and b) cathode Pt/C after the cell tests with reference pattern of Pristine alloy and Mg(OH).

thin (almost unrecognizable low frequency bands). The high frequency −OH mode gives a relative idea about the number of Mg(OH)$_2$ layers formed, as this vibration is composed of in-phase and out-of-phase breathing modes between two adjacent layers.[83] Close-ups of the high frequency peaks from
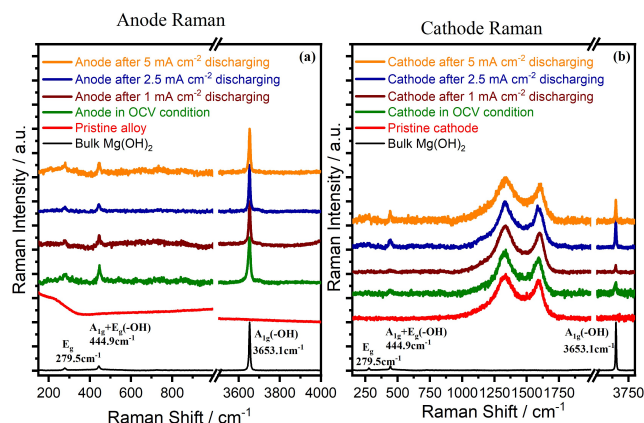
cathodes at different discharge currents, are depicted in Figure 9. The peak for the 5 mA cm^{-2} discharging can be resolved in two separate peaks, centered on 3646 and 3652 cm^{-1} ($A_{1g}^{OH(1)}$ and $A_{1g}^{OH(2)}$), respectively, whereas these two peaks cannot be individually identified for the cathodes cycles at 2.5 mA cm^{-2} and 1 mA cm^{-2}. The presence of the out-of-plane breathing mode in the Raman spectra indicates that there are multiple layers have been deposited on top of 5 mA cm^{-2} discharged cathode. On the other hand, at most a few layers of Mg(OH)$_2$ have formed on top of cathodes discharged by lower current densities.

From these results, we derived that the pH-value must not reach it levels that instigate precipitation of Mg(OH)$_2$ on the electrodes. Following these experiments, the discharge behavior of flow cells was investigated (see Figure S2 in the ESI information for details in the experimental setup). Indeed, we found that, the battery performance can be substantially enhanced, when using the same cathodes in a flow cell design. Figure 10 shows the discharge curves of magnesium-flow cells at different current densities (5, 10 and 20 mA cm^{-2}). In comparison to the previous results, there is no drop of the cell voltage up until the Mg-electrode is fully consumed. These results show the important role of cell design for future applications of aqueous magnesium-air batteries. The Mg$^+$-concentration of the electrolyte after flowing through the cell was approximately at 6.58 ± 0.6 mg$_{Mg2+}$ L^{-1} at a current density of 20 mA cm^{-2}, which is much lower than the determined concentration limit of approx. 20 mg$_{Mg2+}$ L^{-1}. In these tests, only the thickness of the used anode limits the cell performance (see Figure S8 in the ESI).

Conclusion

The pH of the electrolyte plays an important role in the discharge behavior of aqueous magnesium-air batteries. For cells with a stationary electrolyte, we have shown a clear relationship between the Mg^{2+}-concentration, the increase in the pH of electrolyte and the performance drop. A Mg^{2+}
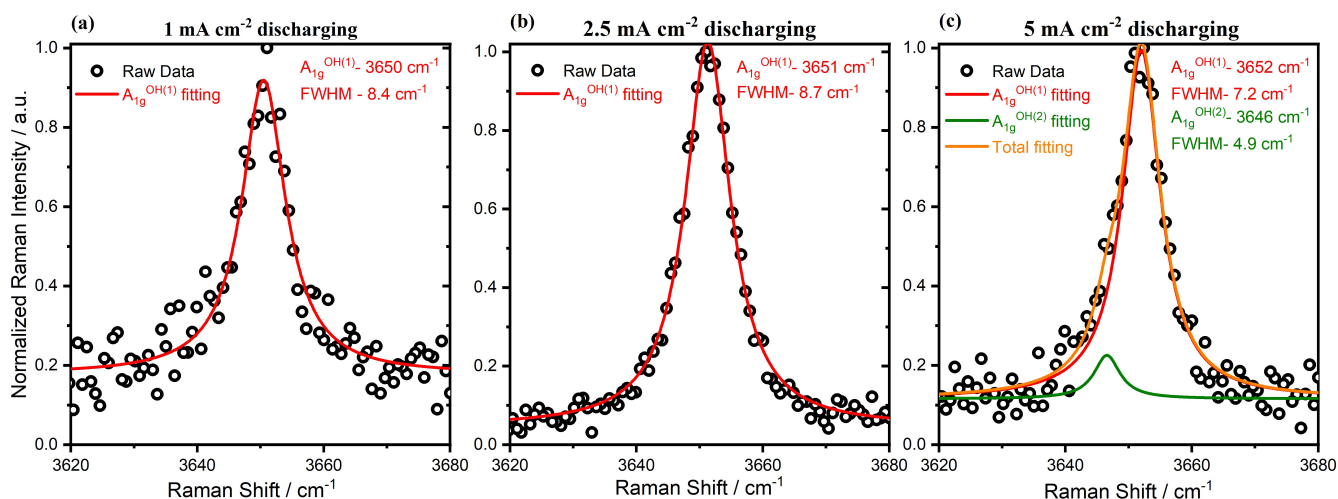
ChemElectroChem

Articles
doi.org/10.1002/celc.202101191

Chemistry
Europe

European Chemical
Societies Publishing

Figure 9. Close-ups of Raman spectra of cathode surfaces at ~3650 cm^{-1}. a) 1 mA cm^{-2} discharging b) 2.5 mA cm^{-2} discharging and c) 5 mA cm^{-2} discharging. Presence of two breathing mode in case of 5 mA cm^{-2} discharging clearly indicates the presence of several layers of Mg(OH)$_2$
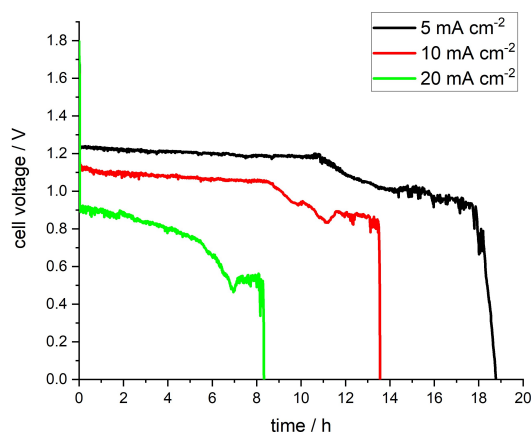

Figure 10. Discharge curves of a magnesium-flow cell at 3 different discharge current densities.

concentration limit of approx. 20 mg L^{-1} was determined, because a decrease in cell performance is observed at higher Mg^{2+} concentrations. For stationary test cells, the poor solubility of magnesium hydroxide limits the function of the entire battery, as a magnesium hydroxide layer is formed everywhere in the test cell after a short time of operation. This acts as a potential passivation layer and blocks the function of the cathode. The slope of the pH depends on the volume of the electrolyte, the size of the electrodes and the discharge current density. By changing the cell design from a stationary electrolyte to a flow cell, the voltage drop could be prevented even with a 6-times higher discharge current density. To achieve high performance aqueous magnesium-air batteries it is necessary to keep the Mg-concentration in the electrolyte small as possible. With a regard to future applications of aqueous magnesium-air batteries, we showed that the best performance will be achieved by use of either big electrolyte reservoirs or in an by design of entirely open systems that allow a continuous exchange of the used electrolyte. The use of additives in the electrolyte to prevent the Mg(OH)$_2$-formation is not a sustainable solution, because amount of additive required would need to be scaled with the battery size.

Experimental Section

Preparation and experimental setup

AZ31 (VWR chemicals, 44011.RF) was cut into pieces 25×25 mm and polished the surface with sandpaper. The alloy was fixed in the anodic current collector. The alloy surface with contact to the electrolyte was 3 cm^2. A gas diffusion layer with mesoporous layer from Freudenberg (H23 C4) with a Pt/C (5 w.–% Pt) catalyst (loading 1 mg cm^{-2}) were cut into 25×20 mm pieces and were fixed in the cathodic current collector with a surface of 3 cm^2. The electrodes had a distance of 13 mm The 0.5 molar NaCl solution was prepared by adding 292.2 g NaCl to 10 L demineralized water. In a typical experiment the cell setup (see Figure S1 in the electronic supporting information, ESI) was placed on a magnetic stirrer with a stir bar inside the electrolyte. 300 mL of the electrolyte was used for the measurements. The oxygen and the nitrogen pressure is kept to 0.8 bar and is used to rinsed the electrolyte.

In the flow-cell setup (see Figure S2 in the ESI) the 0.5 molar NaCl electrolyte was pumped via a peristaltic pump through the cell with a flow rate of 10 mL min^{-1}. The same electrodes were used with an electrolyte contact area of 0.875 cm^2.In addition a Ag/AgCl reference electrode was used. The oxygen supply took place over the ambient air.

Electrolyte characterization

pH-Measurements were done with a pH meter (GMH 5550, GHM Messtechnik GmbH) and the data-log-function where every 30 seconds one data point was recorded.

The Mg content was checked with inductively coupled plasma optical emission spectrometry (ICP-OES, ARCROS SOP, Spectro Analytical Instuments GmbH) measurements. Aliquots a 1 mL were taken after 0, 5, 10, 15, 20, 25, 30, 35, 40, 45, 60, 120, 180, 240 and 300 minutes. The conditions for the ICP-OES measurements are as follows: The plasma power was 1400 W, the cooling gas flow was

ChemElectroChem

Articles
doi.org/10.1002/celc.202101191

Chemistry Europe
European Chemical
Societies Publishing

12 L min^{-1} and the atomizing gas flow was 0.75 L min^{-1}. The detection limit of Mg is 2×10^{-4} mg L^{-1}. The theoretical mass of dissolved Mg is calculated by Faraday equation (10) and the charge Q is defined at constant current by equation (11):

$$Q = m \times z \times F \times M^{-1} \qquad (10)$$

$$Q = I \times t \qquad (11)$$

Where z is the number of electrons involved; F is the Faraday constant; M is the molar mass of Mg; I is the current and t is the time. The theoretical mass of dissolved Mg will be compared with the measured value by ICP.

Electrode characterization

After discharge test both electrodes were investigated by x-ray diffractiometry (XRD, STOE STADI P, Cu-source, STOE & Cie GmbH) for the phase identification of discharge products. The morphology of the used electrodes was observed by scanning electron microscopy (SEM, Zeiss Gimini) with energy-dispersive x-ray (EDX) analysis. In addition, Raman spectra of cathode, anode, alloy material and powdered $Mg(OH)_2$ were collected in the spectral range of 100–4000 cm^{-1} by using an inVia™ confocal Raman microscope (RENISHAW) with a 633 nm excitation laser, 1 mW average laser power and 10 s exposer time. In the confocal system, a grating was used as dispersion element with a groove density of 1800 mm^{-1}, while a 50X (0.75 NA) objective was used in back scattering geometry to collect the Raman spectra.

Electrochemical characterization

The constant current discharge tests were performed with a VMP3 potentiostat from BioLogic. The different discharge current densities (1, 2.5, 5 mA cm^{-2}) were hold for 5 h and every 30 seconds one data point was recorded. The electrochemical performance of the cell was studied in a 0.5 M NaCl-solution at room temperature. Flow cell discharge tests were performed in an analog way.

Acknowledgements

Conflict of Interest

The authors declare no conflict of interest.

[1] F. Cheng, J. Chen, *Chem. Soc. Rev.* **2012**, *41*, 2172–2192.

[2] Q. Liu, Z. Pan, E. Wang, L. An, G. Sun, *Energy Storage Mater.* **2020**, *27*, 478–505.

[3] T. Zhang, Z. Tao, J. Chen, *Mater. Horiz.* **2014**, *1*, 196–206.

[4] B. Peng, J. Liang, Z. Tao, J. Chen, *J. Mater. Chem.* **2009**, *19*, 2877–2883.

[5] A. Atrens, G.-L. Song, F. Cao, Z. Shi, P. K. Bowen, *J. Magnes. Alloys* **2013**, *1*, 177–200.

[6] S. Bender, J. Goellner, A. Heyn, S. Schmigalla, *Mater. Corros.* **2012**, *63*, 707–712.

[7] G. S. Frankel, S. Fajardo, B. M. Lynch, *Faraday Discuss.* **2015**, *180*, 11–33.

[8] T. Zheng, Y. Hu, Y. Zhang, S. Yang, F. Pan, *Mater. Des.* **2018**, *137*, 245–255.

[9] M. Yuasa, X. Huang, K. Suzuki, M. Mabuchi, Y. Chino, *Mater. Trans.* **2014**, *55*, 1202–1207.

[10] N. Wang, R. Wang, Y. Feng, W. Xiong, J. Zhang, M. Deng, *Corros. Sci.* **2016**, *112*, 13–24.

[11] N. Wang, R. Wang, C. Peng, B. Peng, Y. Feng, C. Hu, *Electrochim. Acta* **2014**, *149*, 193–205.

[12] Y. Feng, W. Xiong, J. Zhang, R. Wang, N. Wang, *J. Mater. Chem. A* **2016**, *4*, 8658–8668.

[13] M. Deng, D. Höche, S. V. Lamaka, D. Snihirova, M. L. Zheludkevich, *J. Power Sources* **2018**, *396*, 109–118.

[14] M. Yuasa, X. Huang, K. Suzuki, M. Mabuchi, Y. Chino, *J. Power Sources* **2015**, *297*, 449–456.

[15] Y. Ma, N. Li, D. Li, M. Zhang, X. Huang, *J. Power Sources* **2011**, *196*, 2346–2350.

[16] H. Xiong, H. Zhu, J. Luo, K. Yu, C. Shi, H. Fang, Y. Zhang, *J. Mater. Eng. Perform.* **2017**, *26*, 2901–2911.

[17] H. Xiong, K. Yu, X. Yin, Y. Dai, Y. Yan, H. Zhu, *J. Alloys Compd.* **2017**, *708*, 652–661.

[18] Q. Li, W. Xiong, S. Yu, Y. Liu, J. Li, L. Liu, X. Bi, G. Zhu, E. Liu, Y. Zhao, B. Wang, *J. Mater. Sci.* **2021**, 12789–12802.

[19] Z. Li, H. Wang, J. Li, Y. Zhuang, J. Gao, H. Li, W. Cheng, *Adv. Eng. Mater.* **2020**, *22*, 1901332.

[20] H. Wang, X. Chen, Q. Le, Q. Zou, *Mater. Res. Express* **2021**, *8*, 46521.

[21] X. Chen, Q. Zou, Q. Le, J. Hou, R. Guo, H. Wang, C. Hu, L. Bao, T. Wang, D. Zhao, F. Yu, A. Atrens, *J. Power Sources* **2020**, *451*, 227807.

[22] X. Ren, Q. Lv, L. Liu, B. Liu, Y. Wang, A. Liu, G. Wu, *Sustain. Energy Fuels* **2020**, *4*, 15–30.

[23] H. Cruz-Martínez, H. Rojas-Chávez, P. T. Matadamas-Ortiz, J. C. Ortiz-Herrera, E. López-Chávez, O. Solorza-Feria, D. I. Medina, *Mater. Today Phys.* **2021**, *19*, 100406.

[24] Q. Zhao, C. Wang, H. Wang, J. Wang, Y. Tang, Z. Mao, K. Sasaki, *New J. Chem.* **2020**, *44*, 3728–3736.

[25] A. Mahata, A. S. Nair, B. Pathak, *Catal. Sci. Technol.* **2019**, *9*, 4835–4863.

[26] S. Sui, X. Wang, X. Zhou, Y. Su, S. Riffat, C. Liu, *J. Mater. Chem. A* **2017**, *5*, 1808–1825.

[27] C. Zhang, X. Shen, Y. Pan, Z. Peng, *Front. Energy* **2017**, *11*, 268–285.

[28] H. Cruz-Martínez, M. M. Tellez-Cruz, O. Solorza-Feria, P. Calaminici, D. I. Medina, *Int. J. Hydrogen Energy* **2020**, *45*, 13738–13745.

[29] G. Bampos, L. Sygellou, S. Bebelis, *Catal. Today* **2020**, *355*, 685–697.

[30] L. E. Betancourt, A. Rojas-Pérez, I. Orozco, A. I. Frenkel, Y. Li, K. Sasaki, S. D. Senanayake, C. R. Cabrera, *ACS Appl. Energ. Mater.* **2020**, *3*, 2342–2349.

[31] M. Beltrán-Gastélum, M. I. Salazar-Gastélum, J. R. Flores-Hernández, G. G. Botte, S. Pérez-Sicairos, T. Romero-Castañon, E. Reynoso-Soto, R. M. Félix-Navarro, *Energy* **2019**, *181*, 1225–1234.

[32] G. Darabdhara, M. R. Das, M. A. Amin, G. A. Mersal, N. Y. Mostafa, S. S. Abd El-Rehim, S. Szunerits, R. Boukherroub, *Int. J. Hydrogen Energy* **2018**, *43*, 1424–1438.

[33] T. J. Schmidt, V. Stamenkovic, M. Arenz, N. M. Markovic, P. N. Ross, *Electrochim. Acta* **2002**, *47*, 3765–3776.

[34] J. Wang, F. Chen, Y. Jin, R. L. Johnston, *J. Mater. Chem. A* **2016**, *4*, 17828–17837.

[35] X. Chen, R. Hu, F. Sun, *J. Renew. Sustain. Energy* **2018**, *10*, 054301.

[36] H. Erikson, A. Sarapuu, K. Tammeveski, *ChemElectroChem* **2019**, *6*, 73–86.

[37] M. A. Hernández-Rodríguez, M. C. Goya, M. C. Arévalo, J. L. Rodríguez, E. Pastor, *Int. J. Hydrogen Energy* **2016**, *41*, 19789–19798.

[38] X. Zhong, X. Qin, X. Chen, W. Xu, G. Zhuang, X. Li, J. Wang, *Carbon* **2017**, *114*, 740–748.

[39] J. Wu, S. Shan, H. Cronk, F. Chang, H. Kareem, Y. Zhao, J. Luo, V. Petkov, C.-J. Zhong, *J. Phys. Chem. C* **2017**, *121*, 14128–14136.

[40] L. Cao, Y. Shao, H. Pan, Z. Lu, *J. Phys. Chem. C* **2020**, *124*, 11301–11307.

[41] P. Lang, N. Yuan, Q. Jiang, Y. Zhang, J. Tang, *Energy Technol.* **2020**, *8*, 1900984.

[42] S. N. Goubert-Renaudin, A. Wieckowski, *J. Electroanal. Chem.* **2011**, *652*, 44–51.

[43] R. Sirirak, B. Jarulertwathana, V. Laokawee, W. Susingrat, T. Sarakonsri, *Res. Chem. Intermed.* **2017**, *43*, 2905–2919.

[44] D. M. Morales, M. A. Kazakova, S. Dieckhöfer, A. G. Selyutin, G. V. Golubtsov, W. Schuhmann, J. Masa, *Adv. Funct. Mater.* **2020**, *30*, 1905992.

[45] Y. Xue, S. Sun, Q. Wang, Z. Dong, Z. Liu, *J. Mater. Chem. A* **2018**, *6*, 10595–10626.

[46] X.-H. Yan, P. Prabhu, H. Xu, Z. Meng, T. Xue, J.-M. Lee, *Small Methods* **2020**, *4*, 1900575.

[47] C. Zhu, Q. Shi, B. Z. Xu, S. Fu, G. Wan, C. Yang, S. Yao, J. Song, H. Zhou, D. Du, S. P. Beckman, D. Su, Y. Lin, *Adv. Energy Mater.* **2018**, *8*, 1801956.

[48] M. Song, Y. Song, W. Sha, B. Xu, J. Guo, Y. Wu, *Catalysts* **2020**, *10*, 141.

[49] L. Yang, S. Jiang, Y. Zhao, L. Zhu, S. Chen, X. Wang, Q. Wu, J. Ma, Y. Ma, Z. Hu, *Angew. Chem.* **2011**, *50*, 7132–7135.

[50] L. Wang, H. Dong, Z. Guo, L. Zhang, T. Hou, Y. Li, *J. Phys. Chem. C* **2016**, *120*, 17427–17434.

[51] X. Bo, L. Guo, *Phys. Chem. Chem. Phys.* **2013**, *15*, 2459–2465.

[52] Z. Wu, M. Song, J. Wang, X. Liu, *Catalysts* **2018**, *8*, 196.

[53] M. Wassner, M. Eckardt, A. Reyer, T. Diemant, M. S. Elsaesser, R. J. Behm, N. Hüsing, *Beilstein J. Nanotechnol.* **2020**, *11*, 1–15.

[54] J. C. Carrillo-Rodríguez, I. L. Alonso-Lemus, A. A. Siller-Ceniceros, E. Martínez, G. P. Pizá-Ruiz, G. Vargas-Gutiérrez, F. J. Rodríguez-Varela, *Int. J. Hydrogen Energy* **2017**, *42*, 30383–30388.

[55] L. Xia, H. Huang, Z. Fan, D. Hu, D. Zhang, A. S. Khan, M. Usman, L. Pan, *Mater. Des.* **2019**, *182*, 108048.

[56] N. Zhao, *Int. J. Electrochem. Sci.* **2018**, 10626–10634.

[57] H. Wang, A. Kong, *Mater. Lett.* **2014**, *136*, 384–387.

[58] K. Kakaei, A. Balavandi, *J. Colloid Interface Sci.* **2017**, *490*, 819–824.

[59] J. Zhao, C. R. Cabrera, Z. Xia, Z. Chen, *Carbon* **2016**, *104*, 56–63.

[60] R. Li, Z. Wei, X. Gou, W. Xu, *RSC Adv.* **2013**, *3*, 9978–9984.

[61] J. Wu, Z. Yang, X. Li, Q. Sun, C. Jin, P. Strasser, R. Yang, *J. Mater. Chem. A* **2013**, *1*, 9889–9896.

[62] J. Wu, C. Jin, Z. Yang, J. Tian, R. Yang, *Carbon* **2015**, *82*, 562–571.

[63] M. Klingele, C. Pham, K. R. Vuyyuru, B. Britton, S. Holdcroft, A. Fischer, S. Thiele, *Electrochem. Commun.* **2017**, *77*, 71–75.

[64] F. Böttger-Hiller, A. Mehner, S. Anders, L. Kroll, G. Cox, F. Simon, S. Spange, *Chem. Commun.* **2012**, *48*, 10568–10570.

[65] S. Akula, V. Parthiban, S. G. Peera, B. P. Singh, S. R. Dhakate, A. K. Sahu, *J. Electrochem. Soc.* **2017**, *164*, F568-F576.

[66] S. Akula, B. Balasubramaniam, P. Varathan, A. K. Sahu, *ACS Appl. Energ. Mater.* **2019**, *2*, 3253–3263.

[67] L. M. Rivera, S. Fajardo, M. d. C. Arévalo, G. García, E. Pastor, *Catalysts* **2017**, *7*, 278.

[68] N. A. Anastasijević, V. Vesović, R. R. Adžić, *J. Electroanal. Chem. Interfacial Electrochem.* **1987**, *229*, 305–316.

[69] Q. He, E. J. Cairns, *J. Electrochem. Soc.* **2015**, *162*, F1504-F1539.

[70] S. Sathyanarayana, N. Munichandraiah, *J. Appl. Electrochem.* **1981**, *11*, 33–39.

[71] D. Höche, S. V. Lamaka, B. Vaghefinazari, T. Braun, R. P. Petrauskas, M. Fichtner, M. L. Zheludkevich, *Sci. Rep.* **2018**, *8*, 7578.

[72] B. Winther-Jensen, M. Gaadingwe, D. R. Macfarlane, M. Forsyth, *Electrochim. Acta* **2008**, *53*, 5881–5884.

[73] D. Snihirova, L. Wang, S. V. Lamaka, C. Wang, M. Deng, B. Vaghefinazari, D. Höche, M. L. Zheludkevich, *J. Phys. Chem. Lett.* **2020**, *11*, 8790–8798.

[74] L. Wang, D. Snihirova, M. Deng, C. Wang, D. Höche, S. V. Lamaka, M. L. Zheludkevich, *Electrochim. Acta* **2021**, *373*, 137916.

[75] Y. Zhou, X. Lu, L. Yang, Di Tie, T. Zhang, F. Wang, *Electrochim. Acta* **2021**, *370*, 137805.

[76] Magpowersystems Inc., *http://www.magpowersystems.com/*.

[77] INTERNATIONAL UNION OF PURE AND APPLIED CHEMISTRY, *SOLUBILITY DATA SERIES, Volume 52, ALKALINE EARTH HYDROXIDES IN WATER AND AQUEOUS SOLUTIONS. https://iupac.github.io/SolubilityDataSeries/volumes/SDS-52.pdf*, **1992**.

[78] W. Stumm, J. J. Morgan, *Aquatic chemistry. Chemical equilibria and rates in natural waters*, John Wiley & Sons Inc, New York, Chichester, Brisbane, Toronto, SIngapore, **1996**.

[79] G. Williams, H. Ap Llwyd Dafydd, R. Subramanian, H. N. McMurray, *Corrosion* **2017**, *73*, 471–481.

[80] A. Maltseva, V. Shkirskiy, G. Lefèvre, P. Volovitch, *Corros. Sci.* **2019**, *153*, 272–282.

[81] *Materials Data on Mg(HO)2 by Materials Project*, LBNL Materials Project; Lawrence Berkeley National Laboratory (LBNL), Berkeley, CA (United States), **2020**.

[82] G. Balducci, L. Bravo Diaz, D. H. Gregory, *CrystEngComm* **2017**, *19*, 6067–6084.

[83] A. Suslu, K. Wu, H. Sahin, B. Chen, S. Yang, T. Aoki, S. Horzum, J. Kang, F. M. Peeters, S. Tongay, *Sci. Rep.* **2016**, *6*, 20525.